Applied Catalysis B: Environmental 306 (2022) 121091

Contents lists available at ScienceDirect

Applied Catalysis B: Environmental

journal homepage: www.elsevier.com/locate/apcatb

Synergy between cobalt and nickel on $NiCo_2O_4$ nanosheets promotes peroxymonosulfate activation for efficient norfloxacin degradation

Pengcheng Cai [a,1], Jian Zhao [b,1], Xiaohui Zhang [a], Tianyu Zhang [a], Guiming Yin [a], Shuai Chen [c], Chung-Li Dong [d], Yu-Cheng Huang [d], Yuanyuan Sun [a,*], Dongjiang Yang [a,*], Baoshan Xing [e]

[a] School of Environmental Science and Engineering, State Key Laboratory of Bio-fibers and Eco-textiles, Shandong Collaborative Innovation Center of Marine Bio-based Fibers and Ecological Textiles, Qingdao University, Qingdao 266071, PR China
[b] Institute of Coastal Environmental Pollution Control, and Ministry of Education Key Laboratory of Marine Environment and Ecology, Frontiers Science Center for Deep Ocean Multispheres and Earth System, Ocean University of China, Qingdao 266100, PR China
[c] State Key Laboratory of Coal Conversion, Institute of Coal Chemistry, Chinese Academy of Science, Taiyuan 030001, PR China
[d] Department of Physics, Tamkang University, 151 Yingzhuan Road, New Taipei City 25137, Taiwan
[e] Stockbridge School of Agriculture, University of Massachusetts, Amherst, MA 01003, United States

ARTICLE INFO

Keywords:
$NiCo_2O_4$ nanosheets
Heterogeneous Fenton-like catalysis
Norfloxacin
PMS activation
Degradation

ABSTRACT

Developing an ultraefficient heterogeneous catalyst for peroxymonosulfate (PMS) activation at a wide pH range is a challenge. Herein, ultrathin $NiCo_2O_4$ nanosheets ($NiCo_2O_4$NS, ~1 nm), with the dominant exposure of (311) facet, was designed for PMS activation. The $NiCo_2O_4$NS/PMS system exhibited superior degradation of norfloxacin (NOR) over a wide pH range. The synergistic effects between Ni and Co were the dominant activation mechanism. Compared with Co_3O_4, $NiCo_2O_4$NS adsorb PMS through a unique "bridge" mode, where both Co and adjacent Ni interact with the same O atom in PMS, increasing the number of electron transfer for enhanced breakage of O—O bond. $NiCo_2O_4$NS with high cycling stability, could reach 100% degradation of other typical pollutants, and showed higher degradation performance in actual wastewater. This work unveils the intrinsic origin of the superior activity of Co-Ni spinel oxides for PMS activation for the first time, and demonstrates its application potential for organic contaminants degradation.

1. Introduction

Antibiotics have been widely employed to prevent or cure bacterial infections in human and animals and to accelerate production in animal husbandry and aquaculture [1–3]. Norfloxacin (NOR), as a classical quinolone antibiotic, has an obvious inactivation effect on a series of gram-negative bacilli and gram-positive bacteria [4,5]. The extensive use of NOR has increased environmental concentrations, which has reached the range of ng/L to μg/L in municipal wastewater, and even "mg/L" in pharmaceutical wastewater [6–8]. However, due to its antibacterial activity and biological resistance, it is difficult to be removed by traditional biological wastewater treatment. Advanced oxidation process (AOP) has proven to be an effective technique that utilizes highly reactive radicals to degrade these refractory contaminants [9]. Compared with hydroxyl radical ($^{\bullet}OH$), sulfate radical ($SO_4^{\bullet-}$) generated from the activation of peroxymonosulfate (PMS) is a stronger oxidant because of its higher oxidation potential (2.5–3.1 V) and longer half-life (30–40 μs) [10,11]. PMS activation methods including UV photolysis, electrolysis, heating and ultrasound, suffer from the limitations of high costs, low energy efficiency and complicated equipment. Although carbonaceous catalysts could achieve desired PMS activation efficiency, high catalyst dosage is needed with poor recyclability. Compared with other PMS activation methods, magnetic transitional metal oxides, such as Co-, Fe-, Ni-based oxides have been confirmed as effective PMS activators with high activation efficiency, low dosage and good recovery performance [12].

Among various transitional metal oxides, Co-containing oxide nanomaterials have been taken as preferred PMS activator. In particular, spinel-type Co_3O_4 is more appealing due to its low cost and excellent redox properties, which has been widely applied in the many fields such as energy storage [13], catalytic conversion of new energy [14] and sensor [15]. Doping metal into Co_3O_4 could further increase the activity

* Corresponding authors.
E-mail addresses: sunyy@qdu.edu.cn (Y. Sun), d.yang@qdu.edu.cn (D. Yang).
[1] P. C. and J. Z. contributed equally to this work.

https://doi.org/10.1016/j.apcatb.2022.121091
Received 29 October 2021; Received in revised form 22 December 2021; Accepted 9 January 2022
Available online 19 January 2022

[16,17]. Tian et al. synthesized dandelion-like $NiCo_2O_4$ microspheres for activating PMS to degrade humic acid, and the degradation efficiency can reach more than 90% within 60 min [18]. Zhang et al. synthesized $NiCo_2O_4$ nanoflakes with a thickness of ~20 nm for activating PMS to degrade rhodamine B, which can be completely removed within 40 min [19]. Compared with 3D nanospheres, 2D nanosheets with high proportion of exposed external edge and non-coordination structure can greatly enhance the mass transport, improve the contact between the PMS and surface-active sites, and shorten the pathway between the generated free radical and pollutants, thereby possibly realizing a high PMS catalytic activity. Although $NiCo_2O_4$ with different morphologies has been used for PMS activation, previous works mainly underlined its degradation performance. The mechanism of bimetallic atoms on $NiCo_2O_4$ nanosheets for PMS activation has not received sufficient attention. This greatly hinders the exploration of the origin of high catalytic activity of $NiCo_2O_4$ and development of high-performance catalysts for PMS activation. Moreover, the degradation performance of $NiCo_2O_4$ towards antibiotics is unknown. Especially, the application potential of $NiCo_2O_4$ nanosheets in actual wastewaters is undetermined.

Herein, we hypothesize that the synergistic effect exits between Ni and Co of $NiCo_2O_4$ nanosheets, which could highly enhance PMS activation and NOR removal. To prove the specific synergistic effect, ultrathin magnetic $NiCo_2O_4$ nanosheets ($NiCo_2O_4$NS, ~1 nm) with the dominant exposure of active (311) facet were synthesized by simple annealing hydroxides and its PMS activation for NOR degradation was studied in this work. The main objectives were to investigate (i) NOR degradation performance of $NiCo_2O_4$NS compared with that of Co_3O_4NS; (ii) the intrinsic synergy mechanism between Ni and Co for PMS activation combining experiments and theoretical calculation; (iii) the role of specific reactive species in NOR degradation; and (iv) practical application potential by analyzing biological toxicity of byproducts, NOR degradation under different water chemistries, and the degradation efficiency towards other organic contaminants.

2. Experimental section

2.1. Catalyst synthesis and characterization

Detailed information of the chemicals used is listed in Text S1 in the Supporting Information (SI). The synthesis of $NiCo_2O_4$NS is divided into preparation of $Ni_{1/2}Co_{2/3}(OH)_2$ precursor and the annealing of $Ni_{1/2}Co_{2/3}(OH)_2$. The synthesis process of $Ni_{1/2}Co_{2/3}(OH)_2$ precursor has a slight modification of previous study [20]. Firstly, $CoCl_2{\cdot}6H_2O$, $NiCl_2{\cdot}6H_2O$ and hexamethylene-tetramine (HMT) with a molar ratio of 1:2:36 were mixed with 500 mL deionized water. The solution was continuously refluxed at 95 °C for 5 h under magnetic stirring. Subsequently, $Ni_{1/2}Co_{2/3}(OH)_2$ precursor was placed in a tube furnace, heated to 350 °C at a rate of 2 °C/min, and kept for 2 h. After cooling down, the powder was washed with deionized water and dried. As control samples, the preparation processes of Co_3O_4NS and NiONS that are provided in Text S2. The characterization including X-ray diffraction (XRD), Transmission electron microscopy (TEM), scanning electron microscopy coupled with energy-dispersive X-ray spectroscopy (SEM-EDS), N_2 adsorption/desorption, X-ray photoelectron spectroscopy (XPS), zeta potential, Co K-edge and Ni K-edge extended X-ray absorption fine structure (EXAFS) and Fourier transform (FT) spectra, electrochemical properties, is described in Text S3.

2.2. NOR degradation experiments and analytical methods

NOR degradation experiment was carried out in dark in a 60 mL glass container at 25 °C, which contained 50 mL 20 mg/L NOR solution (This concentration was chosen based on the wastewater treatment plant serving bulk drug manufacturers [21,22]). The pH was adjusted by 0.1 M NaOH and 0.1 M H_2SO_4. After adding 0.05 g/L $NiCo_2O_4$NS, PMS was added to start the reaction. Samples were taken at a scheduled interval, filtered by 0.22-μm filter membrane, and then immediately adding excess saturated sodium thiosulfate to end the reaction. All of the experiments were conducted in triplicate. The information on high performance liquid chromatography (HPLC), inductively coupled plasma optical emission spectrometer (ICP-OES), electron paramagnetic resonance (EPR), and reactive oxygen species capturing experiments are provided in Text S4. The specific test conditions of liquid chromatography triple quadrupole mass spectrometer (LC-MS) are provided in Text S5. The acute toxicity and the chronic toxicity of NOR and its degradation intermediates generated towards aquatic organisms (fish, daphnia, and green algae) was evaluated by ecological structure activity relationship model (ECOSAR) program based on the exposed functional groups to predict toxicity. Specific details are provided in Text S6. Kinetic analysis methods are provided in Text S7. The actual toxicity experiments were not performed because it is different to guarantee the equivalent concentration of the various intermediate products.

2.3. Practical application

The effluent from the secondary sedimentation tank of sewage treatment plant is used as a control to verify the practical application of $NiCo_2O_4$NS. The properties of the used effluent such as biological oxygen demand (BOD), chemical oxygen demand (COD), total nitrogen (TN), total phosphorus (TP), mixed liquor suspended solid (SS), chloride, nitrate, sulfate, bicarbonate and pH were measured. To explore the influence of anions and dissolved organic matter in actual water on the properties of $NiCo_2O_4$NS, NaCl (10 mM), NaH_2PO_4 (10 mM), $NaNO_3$ (10 mM), Na_2SO_4 (10 mM), $NaHCO_3$ (10 mM) and HA (10 mg/L) were selected as experimental variables separately. To explore the wide applicability of $NiCo_2O_4$NS, bisphenol A (BPA), rhodamine B (RhB), sulfamethazine (SMZ), sulfamethoxazole (SMX), tetracycline (TC) and tylosin (TYL) were selected as target pollutants, and their concentrations were determined at the wavelength of 275, 550, 270, 275, 350 and 290 nm by HPLC. Total organic carbon (TOC) contents were determined by a TOC analyzer (TOC-L, Shimadzu, Japan). For the stability evaluation, $NiCo_2O_4$NS was magnetically separated and then washed three times with 1.5 L distilled water, and then dried at 60 °C.

2.4. Calculations

We used the DFT as implemented in the Vienna Ab initio simulation package (VASP) in all calculations [23]. NiO (space group: $Fm\bar{3}m$) and Co_3O_4 (space group: $Fd\bar{3}m$) and $NiCo_2O_4$ (space group: *Imma*) were used to simulate our experiments. The exchange-correlation potential was described by the generalized gradient approximation of Perdew-Burke-Ernzerhof. The projector augmented-wave method is employed to treat interactions between ion cores and valence electrons. The plane-wave cutoff energy was fixed to 500 eV. Given structural models were relaxed until the Hellmann–Feynman forces smaller than − 0.05 eV/Å and the change in energy smaller than 10^{-4} eV was attained. The Brillouin zone with a 2 × 2 × 1 k-point grid was used for structural optimization and frequency calculations, and a 3 × 3 × 3 grid was used for electronic structure calculations. Bader charge analysis was performed to evaluate the charge transfer. To avoid the periodic image interaction between the two nearest neighbor unit cells, the vacuum was set to 20 Å in the z-direction.

3. Results and discussion

3.1. Characterizations of $NiCo_2O_4$NS

TEM image (Fig. 1A and Fig. S1B-C) and XRD pattern (Fig. 1B and Fig. S1A) confirm the successful synthesis of $NiCo_2O_4$NS, Co_3O_4NS and NiONS. TEM results show that $NiCo_2O_4$NS, Co_3O_4NS and NiONS are 2D nanosheet structures. In Fig. 1B, the peaks at 18.9°, 31.2°, 36.7°, 38.4°,

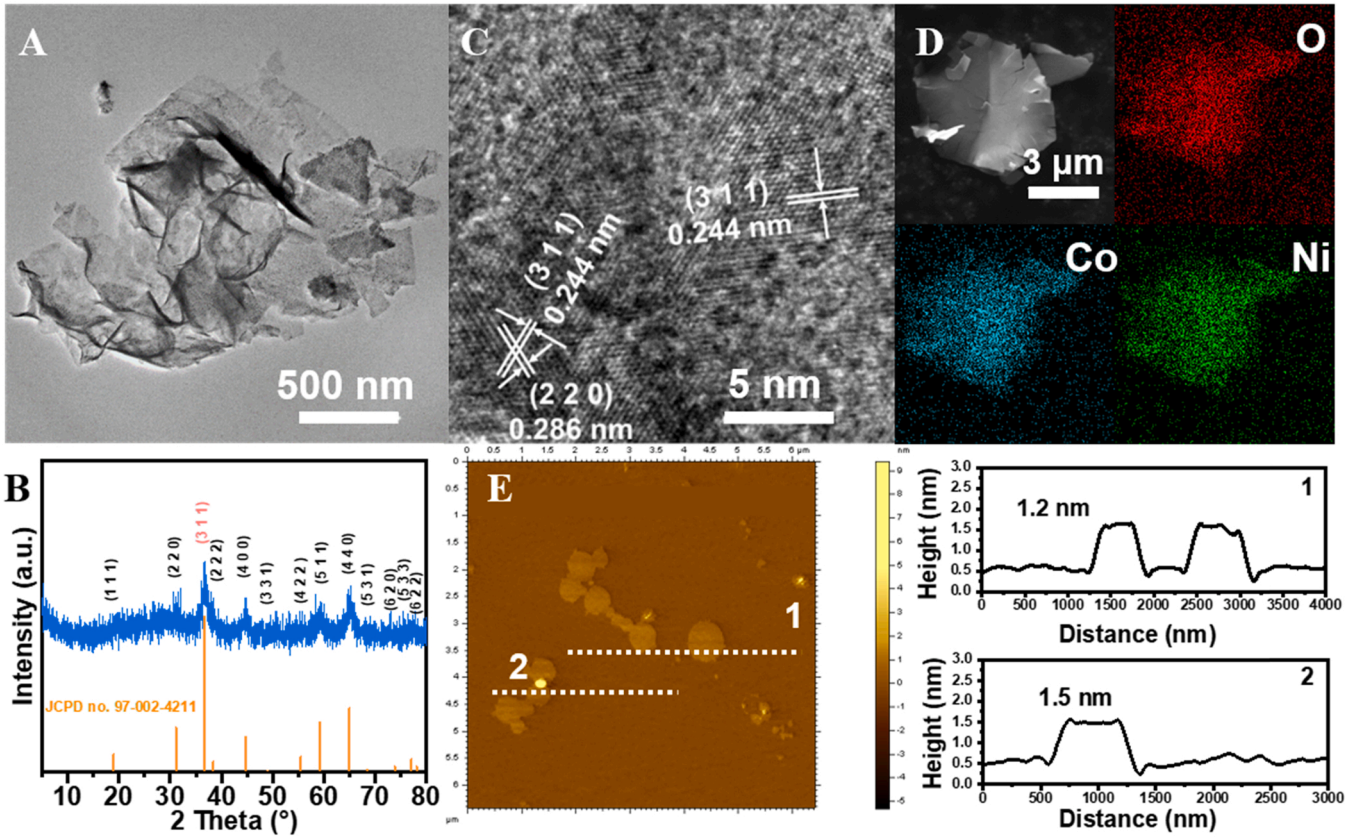

Fig. 1. Characterization of $NiCo_2O_4NS$ (A-E) (A) TEM image; (B) XRD pattern; (C) Lattice fringe of $NiCo_2O_4NS$; (D) EDS mapping; (E) AFM image of $NiCo_2O_4NS$.

44.6°, 48.9°, 55.4°, 59.1° and 64.9° are attributed to $NiCo_2O_4$ facets of (111), (220), (311), (222), (400), (331), (422), (511), (440), respectively. The lattice stripes with the spacing of 0.244 and 0.286 nm are attributed to the dominant exposure of the (311) and (220) facet (Fig. 1C). EDS mapping diagrams (Fig. 1D) demonstrate the uniform distributions of Co, Ni and O elements. The thickness of $NiCo_2O_4NS$ is about 1 nm based on AFM analysis (Fig. 1E). N_2 adsorption-desorption isotherm shows a fast adsorption at low pressure and an obvious hysteresis loop at $P/P_0 > 0.4$ (Fig. S1D), suggesting both the existence of micropore and mesoporous (in the range of 2–6 nm). The specific surface area of $NiCo_2O_4NS$ (102.03 m^2/g) is the highest, followed by Co_3O_4NS (91.75 m^2/g, Fig. S1E), and NiONS (77.07 m^2/g, Fig. S1F). The high specific surface and ultrathin nanosheets could provide more mass transport paths across the nanosheets and exposed active sites, which is favorable for PMS activation.

The cation distribution in spinel is accurately revealed by Fourier transform (FT) of EXAFS. For control sample, Co_3O_4NS, Co occupied both the octahedral and tetrahedral sites. The Co interatomic distances between octahedral sites (TM_{Oct}-TM_{Oct}), tetrahedral sites (TM_{Td}-TM_{Td}) and octahedral-tetrahedral sites (TM_{Oct}-TM_{Td}) are 2.5, 3.0 and 3.0 Å, respectively (Fig. 2A) [24,25]. For $NiCo_2O_4NS$, the peak signals at 2.5 and 3 Å indicate that Co occupies both octahedral and tetrahedral sites. While, FT of Ni K-edge EXAFS spectra (Fig. 2B) displays only a signal peak at 2.5 Å, indicating that Ni only occupies octahedral sites. Therefore, the as-prepared $NiCo_2O_4NS$ is inverse spinel. The chemical states of Ni, Co and O were characterized by XPS (Fig. 2 and Fig. S2). The high-resolution spectrum of O 1s (Fig. 2C) could be divided into three peaks with binding energies at 529.8, 531.1, and 532.1 eV, attributing to lattice oxygen [26], the surface-OH groups [11,27] and the adsorbed H_2O [10,28], respectively. The Ni 2p spectrum of $NiCo_2O_4NS$ (Fig. 2D) was well fitted with two spin-orbit doublets and two satellite satellites. Two spin-orbit binary stars are Ni $2p_{1/2}$ (Ni^{2+} for 872.5 eV and Ni^{3+} for 874.9 eV) and Ni $2p_{3/2}$ (Ni^{2+} for 854.7 eV and Ni^{3+} for 856.5 eV) [29,30]. In Fig. 2E, the Co 2p spectrum was also fitted with two spin-orbit doublets, Co $2p_{1/2}$ (Co^{2+} for 796.7 eV and Co^{3+} for 794.9 eV) and Co $2p_{3/2}$ (Co^{2+} for 781.2 eV and Co^{3+} for 779.7 eV), and two shake-up satellites (786.0 eV and 801.5 eV) [8,13,31,32]. The ratios of mixed-valence Co(II)/Co(III) and Ni(II)/Ni(III) in fresh $NiCo_2O_4NS$ are 61.3/38.7 and 65.2/34.8. By contrast, after $NiCo_2O_4NS$ participated in the reaction, 1.4% of Co(II) and 4.4% of Ni(II) are converted to Co(III) and Ni(III). It is worth noting that the proportion of Co(II) in $NiCo_2O_4NS$ is 14.6% higher than that in Co_3O_4NS, which implies that $NiCo_2O_4NS$ may have higher catalytic activity than Co_3O_4NS.

3.2. NOR degradation by $NiCo_2O_4NS$

The catalytic performance of $NiCo_2O_4NS$ on the degradation of NOR (20 mg/L) was investigated along with control catalysts (Fig. 3A). NOR cannot be degraded in the presence of PMS alone. NOR removal was only 15% in the presence of $NiCo_2O_4NS$ alone, attributing to surface adsorption. Remarkably, in the presence of both $NiCo_2O_4NS$ and PMS, the degradation efficiency of NOR could achieve 97.5% in 90 min. While, the NOR degradation efficiency of NiONS/PMS and Co_3O_4NS/PMS system were only 0.6% and 60.2%, respectively. Compared with Co_3O_4NS, the inactive NiONS and the enhanced efficiency of $NiCo_2O_4NS$, suggest that unique synergistic effects existed between Ni and Co. Furthermore, the catalytic results by homogeneous Co^{2+} (0.811 mg/L, which was equivalent to the concentration detected by ICP after the reaction) in Fig. 3A confirmed that NOR degradation was mainly caused by heterogeneous Fenton catalyzed by $NiCo_2O_4NS$ rather than the leached Co^{2+}.

The effect of $NiCo_2O_4NS$ dosage on NOR degradation is shown in Fig. 3B. When the dosage was 0.5 g/L, nearly complete degradation of NOR achieved within 10 min with a kinetic constant of 0.488 min^{-1}. With the dosage decreased to 0.3, 0.1 and 0.05 g/L, the kinetic constants decreased to 0.168, 0.057, and 0.042 min^{-1}, respectively. The effect of

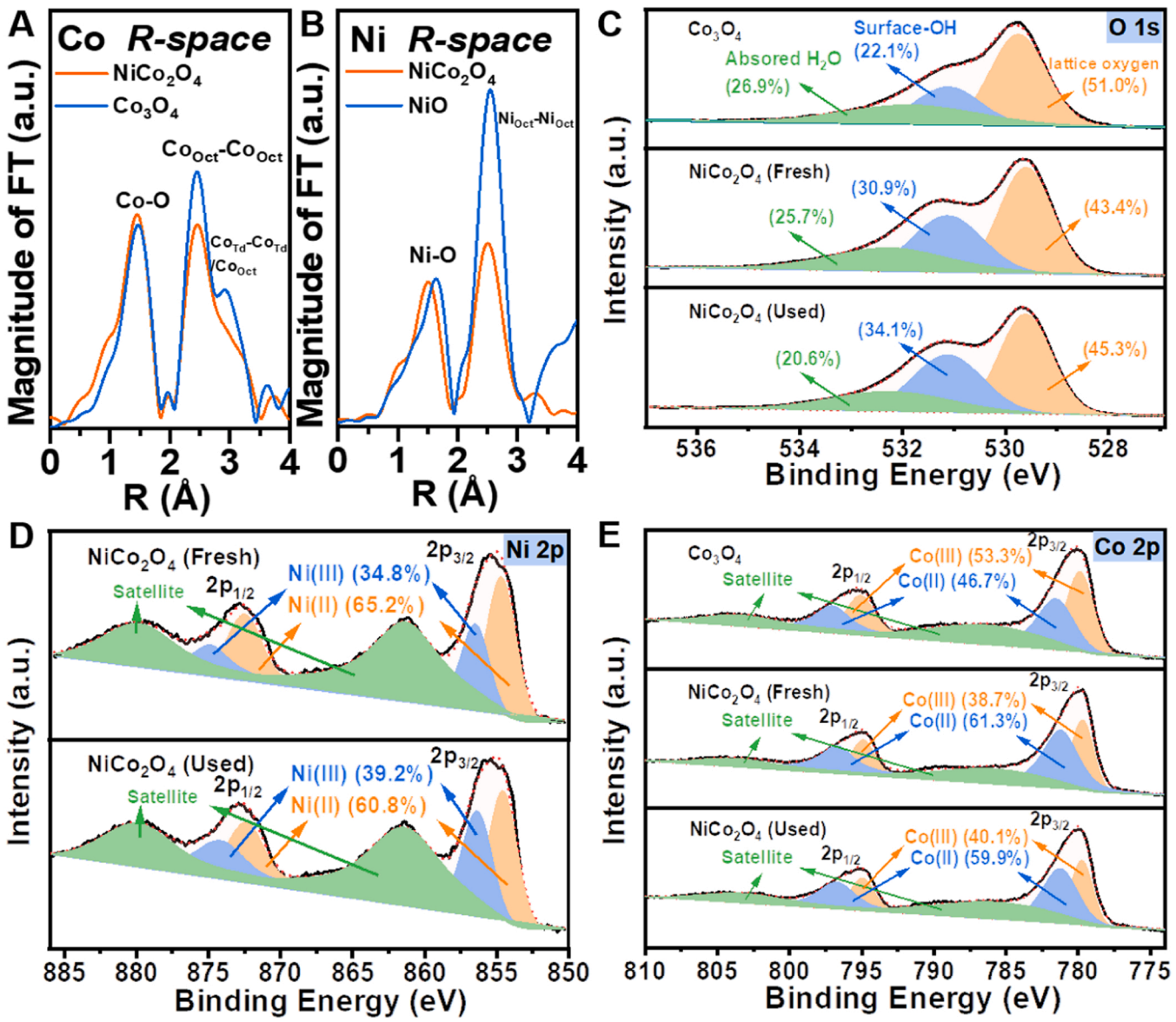

Fig. 2. (A) Fourier transform of Co K-edge EXAFS spectra; (B) Fourier transform of Ni K-edge EXAFS spectra; (C-E) XPS of Co_3O_4NS/$NiCo_2O_4$NS: (C) O 1s; (D) Ni 2p; (E) Co 2p.

PMS concentration on NOR degradation are shown in Fig. S3B. As the PMS concentration increased from 0.333 to 0.667 mM, the degradation rate and degradation efficiency increased. With increasing PMS concentration to 1.0 mM, both degradation rate and degradation efficiency remain constant. The effect of pH on degradation is shown in Fig. 3C. As can be seen, $NiCo_2O_4$NS/PMS system has a strong adaptability to pH, and the degradation efficiency of NOR is higher than 90% at the pH range of 3–11. However, the degradation efficiency of NOR decreases at pH 13, probably because that most of $SO_4^{\bullet-}$ was converted to $^{\bullet}OH$ under strong alkaline condition [33]. Moreover, the isoelectric point of $NiCo_2O_4$NS is 7.22 (Fig. S4). $NiCo_2O_4$NS is positively charged when the pH is less than 7.22, and negatively charged when the pH is greater than 7.22. NOR serves as an amphoteric substance, with the pK_a values of 6.32 and 8.47, respectively [34]. It is mainly present as cations (NOR^+) when pH < 6.32, and anions (NOR^-) when pH > 8.47, or the zwitterionic form ($NOR^{\pm}$/NOR^0) within pH 6.32–8.47. The strong electrostatic repulsion between NOR^- and $NiCo_2O_4$NS results in the unachievable of the NOR^- to the surface of $NiCo_2O_4$NS. This is another reason for the decreased NOR degradation efficiency at pH 13. The pHs before and after the degradation was detected, and shown in Fig. 3C. The introduced $NiCo_2O_4$NS did not change solution pH (Fig. S5). The pH of the solution drops rapidly after adding PMS for 3–5 s, which is attributed to the releases H^+ of PMS after dissolving in water [35]. The information of NOR degradation by several catalysts is displayed in Fig. 3D and Table S1 [36–41]. Among the reported high-activity catalysts for degrading NOR, such as bimetallic spinel oxides, carbon materials, biochar and calcite catalysts, $NiCo_2O_4$NS in our work shows excellent kinetics rate.

3.3. *Mechanism for $NiCo_2O_4$NS surface activation of PMS*

DFT calculations were used to identify the preferential facet and verify advantages of $NiCo_2O_4$NS. In heterogeneous catalytic system, the adsorption of PMS molecules onto the active sites, and subsequent charge transfer between PMS and active sites to break O—O bond in PMS to generate $SO_4^{\bullet-}$ are significant. Thus, it is necessary to calculate the adsorption energy (E_{ads}) and density of states (DOS) between Co/Ni sites and PMS molecules. Based on the TEM results of the exposed (Fig. 1C) and previous reported facets, facets (311), (220), (400) are chosen for PMS adsorption energy calculation. The calculation model is shown in

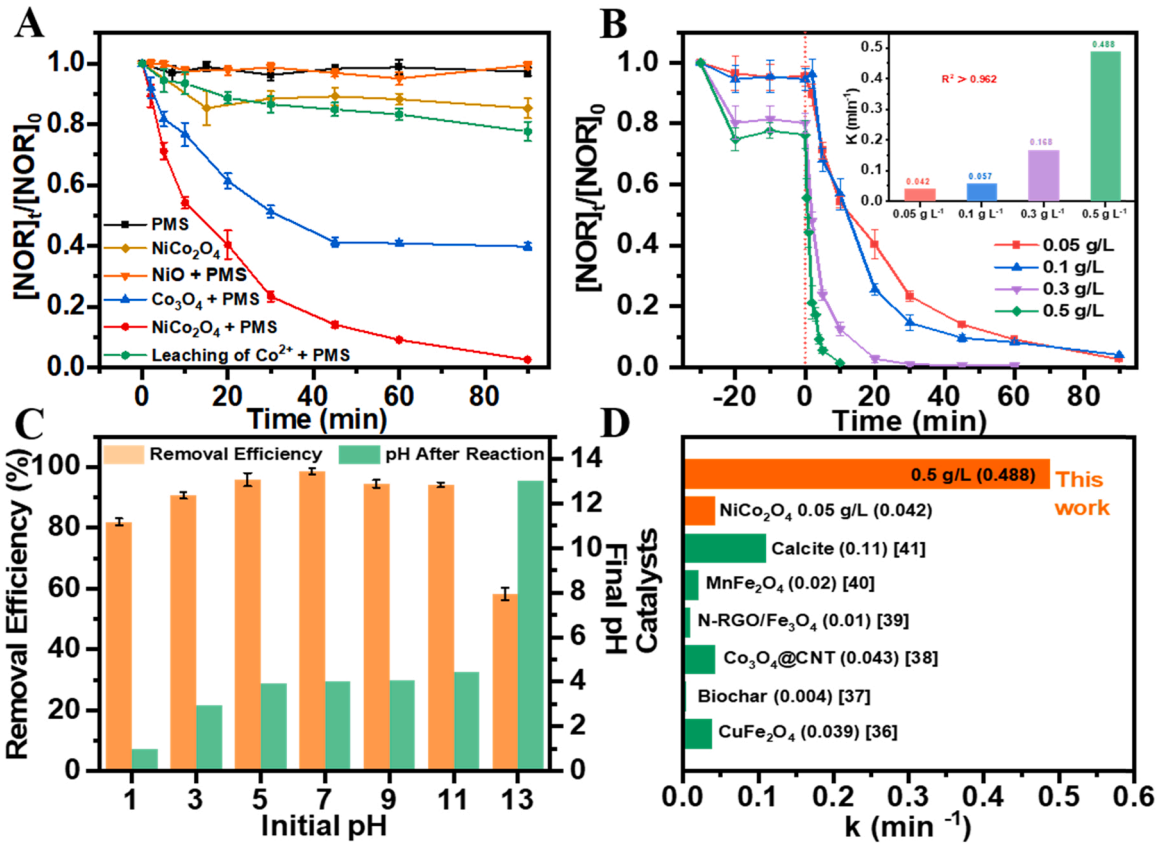

Fig. 3. Performance of $NiCo_2O_4$NS activated PMS. (A) Degradation diagram of NOR; (B) Effect of $NiCo_2O_4$NS dosage on NOR degradation; (C) Effect of initial solution pH on NOR degradation; (D) Comparison of kinetic rate constants of the catalysts for NOR degradation. Experimental conditions unless otherwise specified: $[NOR]_0$ = 20 mg/L, $[PMS]_0$ = 0.667 mM, [Catalysts] = 0.05 g/L, 25 °C, pH = 7.0.

Fig. S6. Fig. 4A shows that $NiCo_2O_4$NS (311) facet has the highest E_{ads} (−3.71 eV) compared with $NiCo_2O_4$NS (400)/(220) facets and NiONS/Co_3O_4NS (311) facet, confirming that the $NiCo_2O_4$NS (311) facet is more favorable for PMS adsorption. The d-band center (−1.430 eV) of NiC-o_2O_4NS is closer to the Fermi level than that of Co_3O_4NS (−1.544 eV) due to Ni occupying (Fig. 4B), which could benefit the catalytic process.

The synergistic effect between Co and Ni site on $NiCo_2O_4$NS (311) facet for PMS activation was surveyed by comparing the differences of adsorption and the charge transfer of Co_3O_4NS and $NiCo_2O_4$NS. The charge density difference of $NiCo_2O_4$NS itself before adsorption of PMS was in Fig. S7. The results demonstrated that O is more inclined to accept electrons from Co_{Oct} site than Co_{Td}/Ni_{Oct} site, indicating that Co_{Oct} plays a leading role in PMS activation. After PMS was introduced, Co_3O_4NS adsorbed PMS molecular through "end-on mode, only one Co active site interacting with the O atom. While, $NiCo_2O_4$ could adsorb PMS molecular through a "bridge" mode, both Co and Ni sites interacting with the same O atom in PMS (Fig. 4C). The results of charge density difference after adsorption of PMS by Co_3O_4NS and $NiCo_2O_4$ are shown in Fig. 4C. Co in Co_3O_4NS transfers 1.292 e to PMS, while Co could transfer more electrons (1.312 e) in $NiCo_2O_4$NS due to increase of the hybridization degree of Co 3d orbitals and O 2p orbitals. Meanwhile, Ni in $NiCo_2O_4$ also could transfer electron (1.044 e) to the same PMS molecule. Thus, the synergistic effect between Ni and Co alters the adsorption mode for PMS, resulting in the increased number of electron transfer for enhanced breakage of O—O bond in PMS.

The CV curves in Fig. 4D showed that the oxidation and reduction peaks of $NiCo_2O_4$NS were more remarkable than that of Co_3O_4NS. The redox potential of $NiCo_2O_4$NS is 1.06 V, and Co_3O_4NS has no obvious redox peak, indicating that $NiCo_2O_4$NS has stronger redox ability than Co_3O_4NS. Meanwhile, the arc radius in the EIS spectrum (Fig. 4E) of $NiCo_2O_4$ is much smaller than that of Co_3O_4NS, suggesting that electrons could be transferred from PMS to Co(III)/Ni(III) centers in $NiCo_2O_4$NS with a faster rate. That's to say, Ni doping can accelerate the electron transmission at the interface and is conducive to the rapid PMS activation.

The quenching experiment and EPR technique were performed to identify the active species in the $NiCo_2O_4$NS/PMS system. Compared with the un-quenched control, the addition of tert-butanol (TB) [14,15, 27] reduced the degradation efficiency of NOR by 6.76% in 90 min (Fig. 5A), indicating that $^{\bullet}OH$ played a minimal role in NOR degradation. However, the addition of ethanol [42] reduced NOR degradation efficiency by 59.3% in 90 min, indicating that the contribution of $SO_4^{\bullet-}$ to NOR degradation was significant. Furthermore, when p-benzoquinone (BQ), a scavenger of $^{\bullet}O_2^-$ [43], was present in NOR solution, the degradation efficiency finally decreased to 56.7% in 90 min, suggesting that BQ could inhibit NOR degradation through preventing the conversion of $^{\bullet}O_2^-$ to $^1O_2$ (see explanation in EPR analysis below). The addition of L-histidine significantly inhibited the degradation, and the degradation efficiency was only 43.3% in 90 min, due to the quenching of $^1O_2$ by L-histidine or the interaction between PMS and L-histidine. Furfuryl alcohol (FFA) is also reported to be a $^1O_2$ quencher [44]. With the increase of FFA concentration from 1 mM to 10 mM, the degradation efficiency of NOR drops sharply from 48.8% to 2.3%, suggesting that $^1O_2$ indeed play a great role in this degradation process.

The EPR analysis results (Fig. 5B) show the signals of DMPOX, an oxide of DMPO with a hyperfine splitting of 1:2:1:2:1:2:1 instead of signal of $SO_4^{\bullet-}$ and $^{\bullet}OH$. The presence of DMPOX is attributed to further oxidation of DMPO [45,46], which implies the excellent catalytic performance of $NiCo_2O_4$NS towards PMS [47]. The characteristic signal of TEMP-$^1O_2$ can be observed obviously, and almost no signal of DMPO-$^{\bullet}O_2^-$ was detected. There are two sources of $^1O_2$, which are the self-decomposition of PMS and the transformation of $^{\bullet}O_2^-$. The

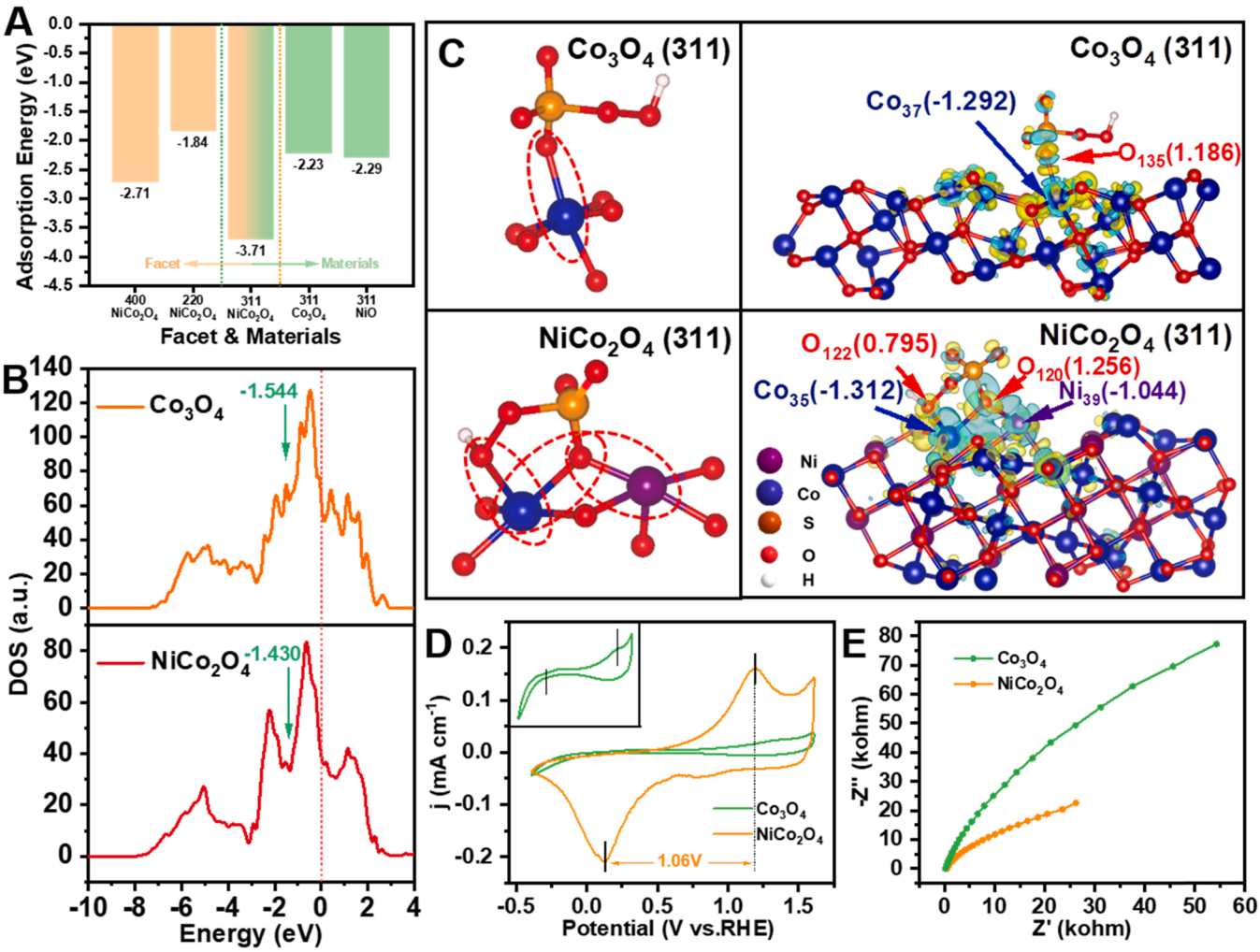

Fig. 4. Mechanism of Ni-Co synergistic enhancement of PMS activation. (A) Adsorption energies of $NiCo_2O_4$NS (400)/(220)/(311) facet and NiONS/Co_3O_4NS (311) facet; (B) The DOS and d-band centers of Co in Co_3O_4NS/$NiCo_2O_4$NS as determined by VASP; (C) Schematic diagram of PMS adsorption by Co_3O_4/$NiCo_2O_4$NS, and charge density difference of PMS adsorption on $NiCo_2O_4$NS and Co_3O_4NS, in which the level of the isosurface is set to 0.006 e $Å^{-3}$; (D) CV curves of Co_3O_4NS and $NiCo_2O_4$NS on GC-RDE (0.116 mg cm^{-2}); (E) EIS spectra of Co_3O_4NS and $NiCo_2O_4$NS.

self-decomposition rate of PMS is low (k = 4.7–5.9 $\times 10^{-2}$ M^{-1} s^{-1} at pH = ~9–10) [48], which often requires the catalysis of quinone [49]. $^1O_2$ was thus mainly produced from $^{\bullet}O_2^-$ transformation in $NiCo_2O_4$NS/PMS system. Therefore, it is confirmed that $SO_4^{\bullet-}$, $^{\bullet}OH$ and $^1O_2$ were the main active species. The relative contribution of $^{\bullet}OH$, $SO_4^{\bullet-}$, and $^1O_2$ was calculated to be 19.16%, 42.52% and 38.32% (The computation process was provided in Supporting Information Text S8 [50]).

The mechanism on NOR degradation in $NiCo_2O_4$NS/PMS system was summarized based on the findings as described above. Firstly, the ≡Co(II)/Ni(II) in $NiCo_2O_4$NS quickly adsorbed and contacted PMS molecules on the surface of $NiCo_2O_4$NS, activated PMS to produce $SO_4^{\bullet-}$ via Eq. (1). According to Text S8 analysis, 42.52% $SO_4^{\bullet-}$ directly participated in the degradation of NOR and the remaining $SO_4^{\bullet-}$ assisted the generation of $^{\bullet}OH$ (Eqs. 2–4). Subsequently, 33.33% $^{\bullet}OH$ was directly involved in the degradation process, while 66.67% $^{\bullet}OH$ would participate in the generation of $^{\bullet}O_2^-$ ($HO_2^{\bullet}$/$^{\bullet}O_2^-$) (Eqs. 5–8) and all $^{\bullet}O_2^-$ directly transformed to $^1O_2$ (Eq. 9) [50]. The regeneration of catalyst depends on the reaction of high valence metal with PMS to produce low valence metal (Eq. 2) and $SO_5^{\bullet-}$, and $SO_5^{\bullet-}$ will continue to decompose into $SO_4^{\bullet-}$ to participate in the above reaction. Moreover, according to the oxidation-reduction potentials of Ni(III)/Ni(II) (≤0.86 V) [51] and Co(III)/Co(II) (1.80 V), Ni(II) reduces Co(III) to Co(II) via Eq. (10). Finally, degradation and mineralization of NOR are realized (Eq. 11).

$$\equiv Co(II)/Ni(II) + HSO_5^- \rightarrow \equiv Co(II)/Ni(II)\text{-}OOSO_3 \rightarrow \equiv Co(III)/Ni(III) + SO_4^{\bullet-} + OH^- \quad (1)$$

$$\equiv Co(III)/Ni(III) + HSO_5^- \rightarrow \equiv Co(III)/Ni(III)\text{-}OOSO_3 \rightarrow \equiv Co(II)/Ni(II) + SO_5^{\bullet-} + H^+ \quad (2)$$

$$2SO_5^{\bullet-} \rightarrow 2SO_4^{\bullet-} + O_2 \quad (3)$$

$$SO_4^{\bullet-} + H_2O \rightarrow {}^{\bullet}OH + H^+ + SO_4^{2-} \quad (4)$$

$$^{\bullet}OH + OH^- \rightarrow O^{\bullet-} + H_2O \quad (5)$$

$$^{\bullet}OH + O^{\bullet-} \rightarrow HO_2^- \quad (6)$$

$$^{\bullet}OH + HO_2^- \rightarrow OH^- + HO_2^{\bullet} \quad (7)$$

$$HO_2^{\bullet} \rightarrow {}^{\bullet}O_2^- + H^+ \quad (8)$$

$$^{\bullet}O_2^- + {}^{\bullet}OH \rightarrow {}^1O_2 + OH^- \quad (9)$$

$$\equiv Ni(II) + \equiv Co(III) \rightarrow \equiv Ni(III) + \equiv Co(II) \quad (10)$$

$$SO_4^{\bullet-}/{}^{\bullet}O_2^-/{}^1O_2 + NOR \rightarrow \text{intermediates} \rightarrow CO_2 + H_2O \quad (11)$$

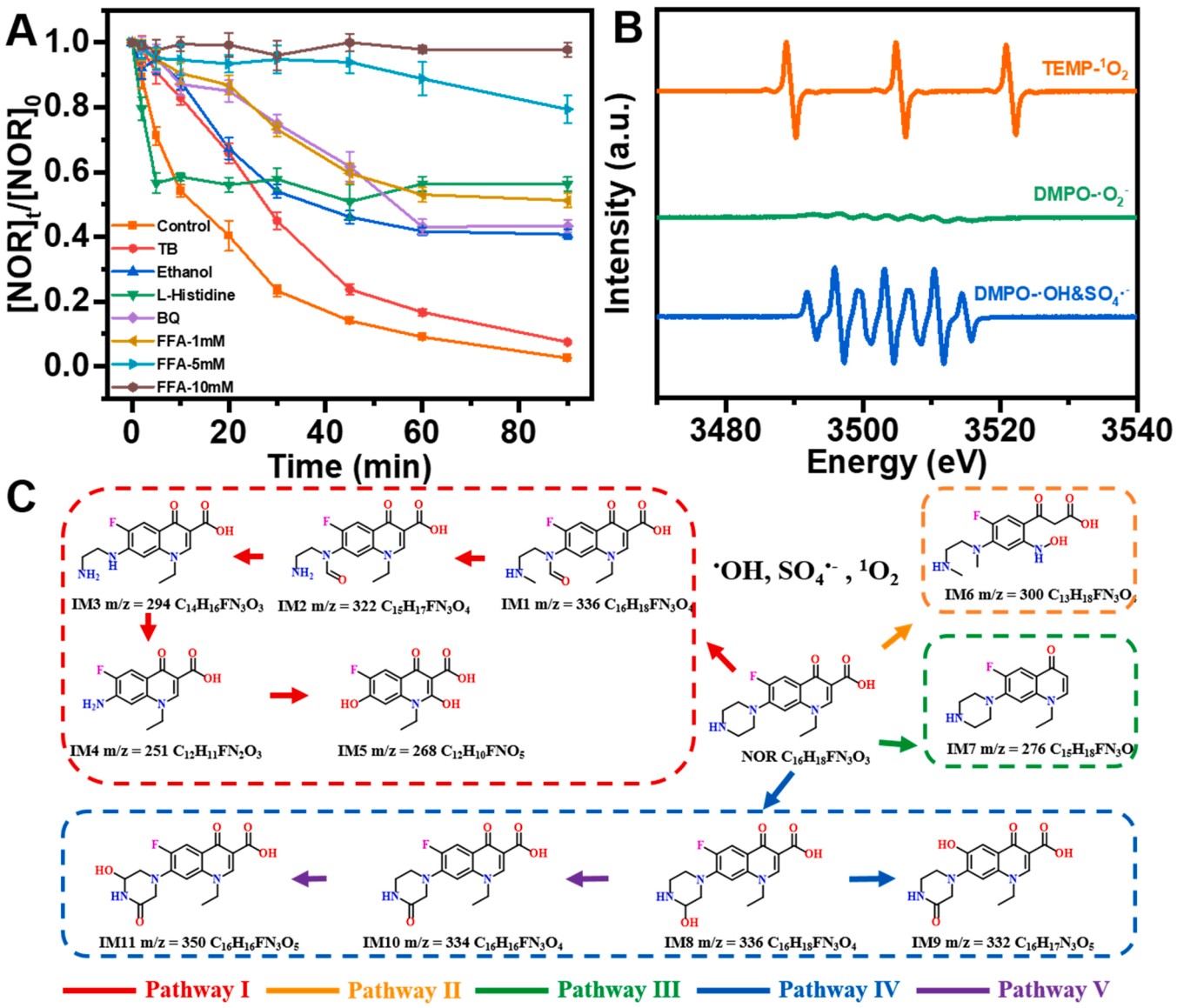

Fig. 5. Determination of active species. (A) Quenching experiment; (B) Electron paramagnetic resonance imaging obtained with DMPO and TEMP as spin-trapping agents. TB, Ethanol and BQ capture $^{\bullet}OH$, $SO_4^{\bullet-}$ and $^{\bullet}O_2^-$, respectively. FFA and L-histidine capture $^1O_2$. (C) Proposed degradation pathway of NOR in $NiCo_2O_4$NS/PMS oxidation system. (The products displayed in the broken-lined brackets indicates no detected in this study but should be exist in the system). Experiment conditions unless otherwise stated: $[NOR]_0$ = 20 mg/L, $[PMS]_0$ = 0.667 mM, [TB] = [Ethanol] = 200 mM, [L-Histidine] = [BQ] = 10 mM, $[NiCo_2O_4NS]$ = 0.05 g/L, 25 °C, pH = 7.0.

3.4. NOR degradation pathways and ecotoxicity of intermediate products

According to LC-MS results, a total of 11 intermediates (*m/z* in range of 251.0836 and 350.1149) were identified and structurally characterized (listed in Table S2). The proposed degradation pathways are shown in Fig. 5C. Pathway I and pathway II are the intermediate reaction of piperazine ring breaking (IM1-IM5) and quinolone ring breaking (IM6). IM1-IM5 were formed through the oxidation and opening of piperazine ring, dealkylation, decarbonylation, depiperazine ring reaction and hydroxylation reaction. IM6 is generated through ring opening reaction of piperazine ring/quinolone ring and hydroxylation. IM7 in pathway III is the decarboxylation product of NOR. Pathway IV mainly represents defluorination reaction and the intermediates IM8 and IM9 were generated through hydroxylation and defluorination. IM10 and IM11 in pathway V are the products of deprotonation and hydroxylation of IM8. Therefore, the degradation process of NOR mainly includes hydroxylation reaction, ring opening reaction of piperazine ring and quinolone ring, decarboxylation and defluorination reaction, and these intermediates are gradually decomposed to benzene ring-containing compounds, and then further oxidized to small organic molecules through ring-opening reaction, finally mineralized into inorganic small molecules.

Because there are no standard substances for these intermediate products, biological toxicity experiments were not performed. Instead, the acute toxicity and the chronic toxicity of NOR and its degradation intermediates towards aquatic organisms were evaluated by ECOSAR program based on the exposed functional groups. And the results are given in Table S3 and Table S4. Overall, most of the intermediates such as IM1/IM2/IM3/IM6/IM8/IM10/IM11 (Fig. 6) are harmless products without acute and chronic toxicity. In the prediction of acute toxicity, IM4/IM5/IM9 intermediates are harmful, only IM7 is toxic. Similarly, in the prediction of chronic toxicity, IM7/IM9 is harmful and IM4/IM7 is toxic to daphnia. None intermediate is toxic to fish and algae. Due to the exposure of the groups of anilines (unhindered) and phenols, the IM4 and IM5 are harmful. Although the exposed groups of IM7 have not changed, the structural changes also cause the increase of the toxicity of

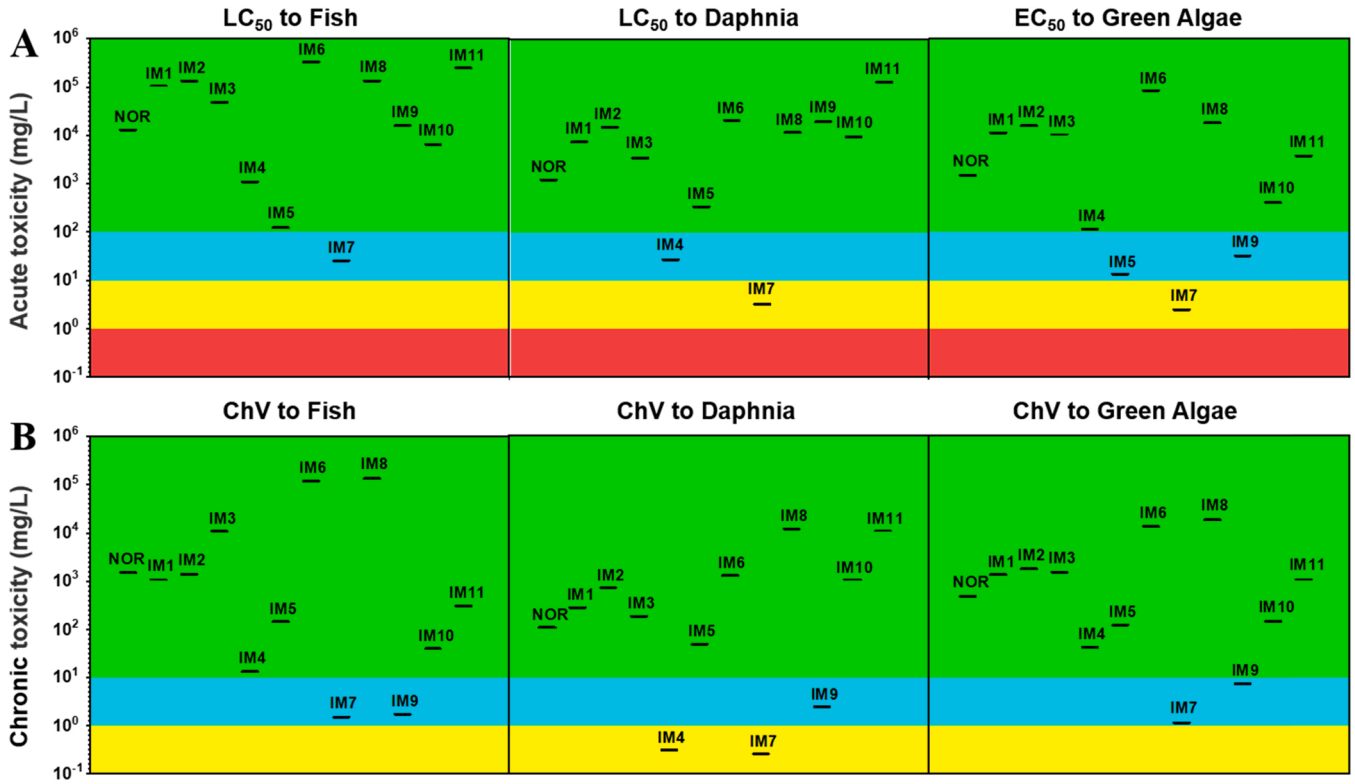

Fig. 6. Acute toxicity (A) and chronic toxicity (B) for NOR and its degradation intermediates generated. Green means harmless, sky blue means harmful, yellow means toxic, and red means highly toxic. LC_{50}: Lethal Concentration 50; EC_{50}: concentration for 50% of maximal effect; ChV: Chronic Value.

the aliphatic amines. The toxicity of IM9 is attributed to the phenolic amine group. Therefore, it is necessary to control the degradation pathway. For example, decarboxylation and defluorination should be avoided to expose more toxic groups (anilines-unhindered, vinyl/allyl/propargyl alcohols-unhindered and phenol amines). Meanwhile, the toxicity of byproducts could be highly lowered by prolonging the degradation time and improving the mineralization degree.

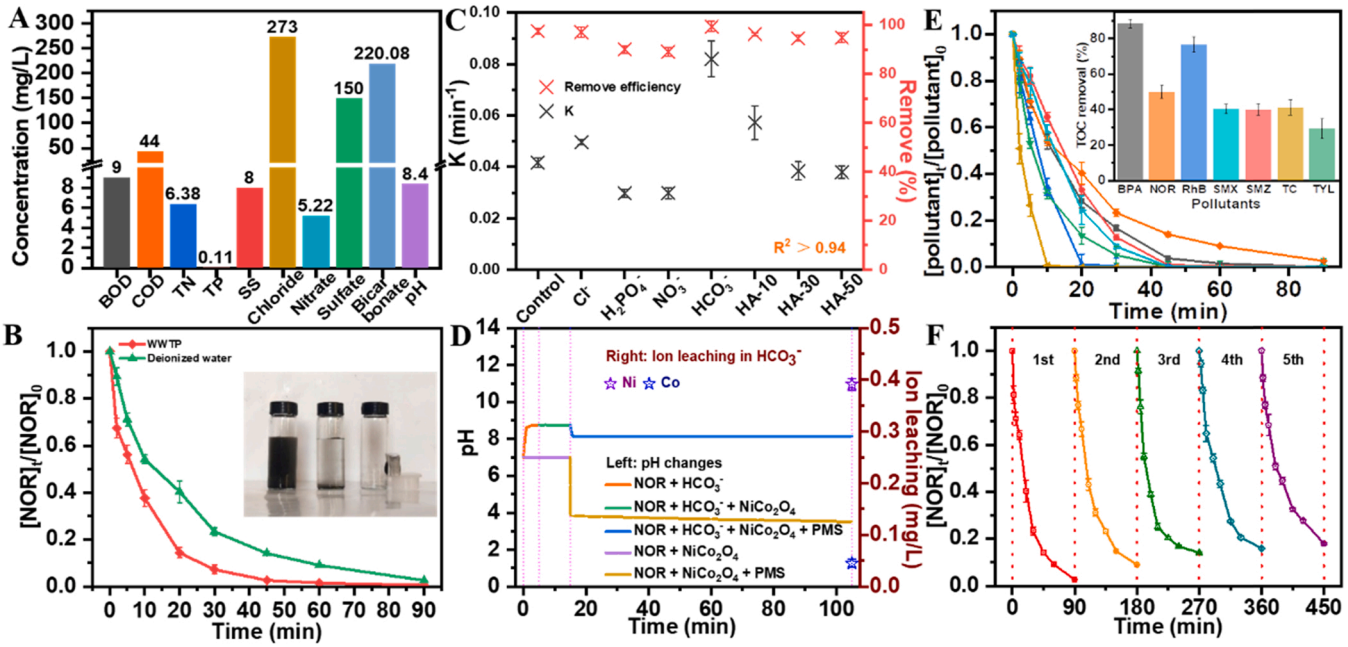

Fig. 7. (A) Effluent water quality of sewage treatment plant; (B) Comparison of NOR degradation efficiency when effluent from sewage treatment plant and deionized water are used as water matrix respectively (insert: the photo of magnetic separation); (C) Effect of anions in water on degradation efficiency of NOR; (D) Change of pH of solution in $NiCo_2O_4NS/PMS/NaHCO_3$ system; (E) Degradation efficiency of different organic pollutants and TOC in the $PMS/NiCo_2O_4NS$ system; (F) Cyclic experiment. Experiment conditions: $[Pollutant]_0 = 20$ mg/L, $[PMS]_0 = 0.667$ mM, $[NiCo_2O_4NS] = 0.05$ g/L, $[Cl^-] = [H_2PO_4^-] = [NO_3^-] = [HCO_3^-] = 10$ mM, $[HA] = 10$ mg/L, 25 °C, pH = 7.0.

3.5. Practical application of $NiCo_2O_4$NS/PMS system

Wastewater contains a series of inorganic ions and organic pollutants. Thus, to evaluate the practical application of the $NiCo_2O_4$NS/PMS system, the degradation performance of NOR in the presence of inorganic ions and secondary wastewater (The water quality conditions are given in Fig. 7A) was explored. Fig. 7B shows that NOR can be completely removed within 90 min in actual wastewater and the catalysts could be easily separated from water by using external magnetic field (Fig. S8, insert in Fig. 7A). Further anion experiment showed that $H_2PO_4^-$ and NO_3^- had an inhibition on NOR degradation because the active radicals were quenched by $H_2PO_4^-$ (Eqs. 12 and 13) [52–54], resulting in the formation of low active radicals. Similarly, NO_3^- could react with $SO_4^{\bullet-}$ to form $NO_3^{\bullet}$ ($E_0 = 2.30$ V) and NO_2·($E_1 = 1.03$ V) with lower redox potential (Eqs. 14 and 15) [55,56]. $H_2PO_4^-$ and NO_3^- anions widely exist in actual wastewater. However, the degradation performance of NOR could be enhanced (Fig. 7B) duo to the co-existence of other promoting substances such as Cl^-, HCO_3^- and organic matter. Cl^- slightly enhanced NOR degradation (Fig. 7C), because Cl^- could be converted into $Cl^{\bullet}$ (Eq. 16) [57] and then generates HOCl and Cl_2 through chain reaction (Eqs. S5–S9) [58,59]. Then, the generated Cl_2 and HOCl could react with HSO_5^- through charge transfer (Eqs. S10, S11) to promote the degradation [22,23].

$$SO_4^{\bullet-} + H_2PO_4^- \rightarrow SO_4^{2-} + H_2PO_4^{\bullet} \quad (12)$$

$$^{\bullet}OH + H_2PO_4^- \rightarrow OH^- + H_2PO_4^{\bullet} \quad (13)$$

$$SO_4^{\bullet-} + NO_3^- \rightarrow SO_4^{2-} + NO_3^{\bullet} \quad (14)$$

$$NO_3^{\bullet} + H_2O + e_{aq}^- \rightarrow NO_2^{\bullet} + 2OH^- \quad (15)$$

$$SO_4^{\bullet-} + Cl^- \leftrightarrow SO_4^{2-} + Cl^{\bullet} \quad (16)$$

Generally, HCO_3^- was previously considered as a radical quencher (Eqs. S12, S13), which may inhibit NOR degradation. However, recent studies reported that $NaHCO_3$ can accelerate the pollutant degradation in homogeneous and heterogeneous AOPs [15,60,61]. To fully reveal the role of $NaHCO_3$, pH variation was monitored. The results showed that the solution pHs in $NiCo_2O_4$NS/PMS system in the presence of $NaHCO_3$ were maintained at 8.1 (Fig. 7D), while the pHs in the absence of $NaHCO_3$ rapidly reduced to 3.8. Consequently, there is no doubt that the stable pH is responsible for the preferable performance of $NiCo_2O_4$NS/PMS/$NaHCO_3$ system. Moreover, HCO_3^- often complexed with metal sites on the $NiCo_2O_4$NS surface [62–64], which shows high reactivity to aromatic compounds through single electron transfer and hydrogen extraction mechanism [59–65]. In the presence of humic acid, the K value increased by 30% (Fig. 7C) because that humic acid could also form complex with $NiCo_2O_4$NS. This complex might act as a potential electron donor to activate PMS [66]. With increasing humic acid concentration to 30 mg/L, even to 50 mg/L, the degradation of NOR is slightly inhibited, which is mainly caused by the partly consumption of active species by the high concentration of humic acid [67]. Therefore, it is confirmed that the enhanced performance of $NiCo_2O_4$NS/PMS system in actual wastewater than in deionized water is attributed to the presence of co-existing anions (Cl^-, HCO_3^-) or low-concentration dissolved organic matter.

In Fig. 7E, the degradation performance of $NiCo_2O_4$/PMS for different organic pollutants is evaluated. The degradation of sulfonamides (SMZ, SMX), macrolide antibiotics (TYL) and tetracycline antibiotics (TC) reached 100% within 90 min. In addition to antibiotics, RhB and BPA, were completely degraded within 90 min. The TOC degradation efficiency for TC, TYL, RhB, SMX, SMZ and NOR was 41.1%, 29.0%, 76.6%, 40.1%, 39.8% and 49.9% after 90 min incubation. The reusability of $NiCo_2O_4$NS was investigated using cycling experiments. It still maintained well degradation efficiency for NOR after five cycles. The NOR degradation efficiency slightly decreased to 90.94%, 85.77%, 84.09%, and 81.45% for the second, third, fourth, and fifth degradation cycles (Fig. 7F). The XRD pattern (Fig. S9) shows that the crystalline phase of $NiCo_2O_4$NS after five cycles was still preserved.

4. Conclusions

The synergy between Co and Ni in $NiCo_2O_4$ nanosheets for PMS activation was explored for the first time. Compared with Co_3O_4 adsorbed PMS molecules through "end-on" mode, $NiCo_2O_4$ could adsorb PMS through a novel "bridge" mode, where both Co and adjacent Ni sites simultaneously interacted with the same O atom in PMS, increasing the number of electron transfer for the breakage of O—O bond. Such a synergistic effect substantially accelerated the catalytic degradation of NOR from 60.2% to 97.5%. It also had a broad spectrum to degrade other typical pollutants (100% degradation of bisphenol A, rhodamine B, sulfamethazine, tetracycline, sulfamethoxazole, tylosin), and showed higher degradation performance in actual wastewater due to the presence of Cl^-/HCO_3^- and organic matter. The final degradation products have no chronic or acute toxicity except IM4/IM7. Moreover, the $NiCo_2O_4$NS with high cycling stability was environmental-friendly, and magnetically separable. Thus, $NiCo_2O_4$NS show promising practical application in actual wastewater treatment. Importantly, the revealed mechanism in this work could provide important implications for designing bimetallic-based catalysts with bimetallic active sites (e.g., carbides, nitrides) for practical Fenton-like applications.

CRediT authorship contribution statement

Pengcheng Cai: Methodology, Formal analysis, Investigation, Data curation, Writing – original draft, Visualization. **Jian Zhao**: Conceptualization, Methodology, Validation, Investigation. **Xiaohui Zhang**: Software, Formal analysis. **Tianyu Zhang**: Data curation, Validation, Investigation. **Guiming Yin**: Data curation, Validation. **Shuai Chen**: Resources, Visualization. **Chung-Li Dong**: Resources, Investigation. **Yu-Cheng Huang**: Resources, Investigation. **Yuanyuan Sun**: Conceptualization, Supervision. **Dongjiang Yang**: Validation, Supervision. **Baoshan Xing**: Writing – reviewing and editing.

Declaration of Competing Interest

The authors declare that they have no known competing financial interests or personal relationships that could have appeared to influence the work reported in this paper.

Acknowledgements

This work is financially support by the National Natural Science Foundation of China, China (51808303, 41822705 and 52102362), Natural Science Foundation of Shandong Province, China (ZR2019BEE027), Science and Technology Support Plan for Youth Innovation of Colleges in Shandong Province, China (DC2000000961), Taishan Scholar Program, China (ts201712030) and State Key Laboratory of Bio-Fibers and Eco-Textiles, China (Qingdao University, ZKT25, ZKT30 and ZFZ201809).

Appendix A. Supporting information

Supplementary data associated with this article can be found in the online version at doi:10.1016/j.apcatb.2022.121091.

References

[1] R.H. Lindberg, P. Wennberg, M.I. Johansson, M. Tysklind, B.A.V. Andersson, Screening of human antibiotic substances and determination of weekly mass flows in five sewage treatment plants in Sweden, Environ. Sci. Technol. 39 (2005) 3421–3429.

[2] M.J. Benotti, R.A. Trenholm, B.J. Vanderford, J.C. Holady, B.D. Stanford, S. A. Snyder, Pharmaceuticals and endocrine disrupting compounds in U.S. drinking water, Environ. Sci. Technol. 43 (2009) 597–603.
[3] Q. Schiermeier, Studies assess risks of drugs in water cycle, Nature 424 (2003) 5.
[4] B. Yan, C.H. Niu, Adsorption behavior of norfloxacin and site energy distribution based on the Dubinin-Astakhov isotherm, Sci. Total Environ. 631–632 (2018) 1525–1533.
[5] K. Oberle, M.J. Capdeville, T. Berthe, H. Budzinski, F. Petit, Evidence for a complex relationship between antibiotics and antibiotic-resistant Escherichia coli: from medical center patients to a receiving environment, Environ. Sci. Technol. 46 (2012) 1859–1868.
[6] X.D. Jin, X.Q. Zhou, P. Sun, S.Y. Lin, W.B. Cao, Z.F. Li, W.X. Liu, Photocatalytic degradation of norfloxacin using N-doped TiO_2: optimization, mechanism, identification of intermediates and toxicity evaluation, Chemosphere 237 (2019), 124433.
[7] T.Q. Yu, Q.L. Xu, G.F. Qian, J.L. Chen, H. Zhang, L. Luo, S.B. Yin, Amorphous CoO_x decorated crystalline RuO_2 nano-sheets as bifunctional catalyst for boosting overall water splitting at large current density, ACS Sustain. Chem. Eng. 8 (2020) 17520–17526.
[8] N.L. Millar, S. Siebert, I.B. McInnes, Europe rules on harm from fluoroquinolone antibiotics, Nature 566 (2019) 326.
[9] C.S. Bao, J. Zhao, Y.Y. Sun, X.L. Zhao, X.H. Zhang, Y.K. Zhu, X.L. She, D.J. Yang, B. S. Xing, Enhanced degradation of norfloxacin by Ce-mediated Fe-MIL-101: catalytic mechanism, degradation pathways, and potential applications in wastewater treatment, Environ. Sci. -Nano 8 (2021) 2347–2359.
[10] Y. Qin, F. Song, Z. Ai, P. Zhang, L. Zhang, Protocatechuic acid promoted alachlor degradation in Fe(III)/H_2O_2 Fenton system, Environ. Sci. Technol. 49 (2015) 7948–7956.
[11] M. Xing, W. Xu, C. Dong, Y. Bai, J. Zeng, Y. Zhou, J. Zhang, Y. Yin, Metal sulfides as excellent Co-catalysts for H_2O_2 decomposition in advanced oxidation processes, Chem 4 (2018) 1359–1372.
[12] J. Lee, U. von Gunten, J.H. Kim, Persulfate-based advanced oxidation: critical assessment of opportunities and roadblocks, Environ. Sci. Technol. 54 (2020) 3064–3081.
[13] S. Sun, D.W. Rao, T. Zhai, Q. Liu, H. Huang, B. Liu, H.S. Zhang, L. Xue, H. Xia, Synergistic interface-assisted electrode-electrolyte coupling toward advanced charge storage, Adv. Mater. 32 (2020), 2005344.
[14] G.F. Qian, J.L. Chen, T.Q. Yu, L. Luo, S.B. Yin, N-doped graphene-decorated NiCo alloy couple with mesoporous NiCoMoO nano-sheets heterojunction for enhanced water electrolysis activity at high current density, Nano-Micro Lett. 13 (2021) 77.
[15] B.H. Sun, H. Lv, Z. Liu, J. Wang, X. Bai, Y. Zhang, J.K. Chen, K. Kan, K.Y. Shi, Co_3O_4@PEI/$Ti_3C_2T_x$ MXene nanocomposites for a highly sensitive NO_x gas sensor with a low detection limit, J. Mater. Chem. A 9 (2021) 6335–6344.
[16] X.Y. Liu, D. Xu, D.F. Zhang, G.Z. Zhang, L. Zhang, Superior performance of 3D Co-Ni bimetallic oxides for catalytic degradation of organic dye: investigation on the effect of catalyst morphology and catalytic mechanism, Appl. Catal. B-Environ. 186 (2016) 193–203.
[17] M.J. Kang, H. Park, J. Jegal, S.Y. Hwang, Y.S. Kang, H.G. Cha, Electrocatalysis of 5-hydroxymethylfurfural at cobalt based spinel catalysts with filamentous nanoarchitecture in alkaline media, Appl. Catal. B-Environ. 242 (2019) 85–91.
[18] X.K. Tian, C. Tian, Y.L. Nie, C. Dai, C. Yang, N. Tian, Z.X. Zhou, Y. Li, Y.X. Wang, Controlled synthesis of dandelion-like $NiCo_2O_4$ microspheres and their catalytic performance for peroxymonosulfate activation in humic acid degradation, Chem. Eng. J. 331 (2018) 144–151.
[19] W.W. Zhang, Y. Su, X.M. Zhang, Y. Yang, X.H. Guo, Facile synthesis of porous $NiCo_2O_4$ nanoflakes as magnetic recoverable catalysts towards the efficient degradation of RhB, RSC Adv. 6 (2016) 64626–64633.
[20] F. Song, X.L. Hu, Exfoliation of layered double hydroxides for enhanced oxygen evolution catalysis, Nat. Commun. 5 (2014) 4477.
[21] D.G.J. Larsson, C. de Pedro, N. Paxeus, Effluent from drug manufactures contains extremely high levels of pharmaceuticals, J. Hazard. Mater. 148 (2007) 751–755.
[22] M.C. Danner, A. Robertson, V. Behrends, J. Reiss, Antibiotic pollution in surface fresh waters: occurrence and effects, Sci. Total Environ. 664 (2019) 793–804.
[23] W. Kohn, L.J. Sham, Self-consistent equations including exchange and correlation effects, Phys. Rev. 140 (1965) A1133–A1138.
[24] E.C. O'Quinn, J. Shamblin, B. Perlov, R.C. Ewing, J. Neuefeind, M. Feygenson, I. Gussev, M. Lang, Inversion in $Mg_{1-x}Ni_xAl_2O_4$ spinel: new insight into local structure, J. Am. Chem. Soc. 139 (2017) 10395–10402.
[25] Y. Zhou, S.N. Sun, C. Wei, Y.M. Sun, P.X. Xi, Z. Feng, Z.J. Xu, Significance of engineering the octahedral units to promote the oxygen evolution reaction of spinel oxides, Adv. Mater. 31 (2019), 1902509.
[26] L. Qian, L. Gu, L. Yang, H.Y. Yuan, D. Xiao, Direct growth of $NiCo_2O_4$ nanostructures on conductive substrates with enhanced electrocatalytic activity and stability for methanol oxidation, Nanoscale 5 (2013) 7388–7396.
[27] Y.E. Roginskaya, O.V. Morozova, E.N. Lubnin, Y.E. Ulitina, G.V. Lopukhova, S. Trasatti, Characterization of bulk and surface composition of $Co_xNi_{1-x}O_y$ mixed oxides for electrocatalysis, Langmuir 13 (1997) 4621–4627.
[28] C.H. An, Y.J. Wang, Y.N. Huang, Y.N. Xu, L.F. Jiao, H.T. Yuan, Porous $NiCo_2O_4$ nanostructures for high performance supercapacitors via a microemulsion technique, Nano Energy 10 (2014) 125–134.
[29] F.X. Ma, L. Yu, C.Y. Xu, X.W. Lou, Self-supported formation of hierarchical $NiCo_2O_4$ tetragonal microtubes with enhanced electrochemical properties, Energy Environ. Sci. 9 (2016) 862–866.
[30] H.L. Wang, C.B. Holt, Z. Li, X. Tan, B. Amirkhiz, Z. Xu, B. Olsen, T. Stephenson, D. Mitlin, Graphene-nickel cobaltite nanocomposite asymmetrical supercapacitor with commercial level mass loading, Nano Res. 5 (2012) 605–617.
[31] J.G. Kim, D.L. Pugmire, D. Battaglia, M.A. Langell, Analysis of the $NiCo_2O_4$ spinel surface with Auger and X-ray photoelectron spectroscopy, Appl. Surf. Sci. 165 (2000) 70–84.
[32] Y. Gao, Q. Wang, G.Z. Ji, A.M. Li, Degradation of antibiotic pollutants by persulfate activated with various carbon materials, Chem. Eng. J. 429 (2022), 132387.
[33] H. Wu, X.J. Niu, J. Yang, C.H. Wang, M.Q. Lu, Retentions of bisphenol A and norfloxacin by three different ultrafiltration membranes in regard to drinking water treatment, Chem. Eng. J. 294 (2016) 410–416.
[34] C.J. Liang, Z.S. Wang, C.J. Bruell, Influence of pH on persulfate oxidation of TCE at ambient temperatures, Chemosphere 66 (2007) 106–113.
[35] J.H. Ji, R.M. Aleisa, H. Duan, J.L. Zhang, Y.D. Yin, M.Y. Xing, Metallic active sites on MoO_2(110) surface to catalyze advanced oxidation processes for efficient pollutant removal, iScience 23 (2020), 100861.
[36] Y.R. Wang, D.F. Tian, W. Chu, M.R. Li, X.W. Lu, Nanoscaled magnetic $CuFe_2O_4$ as an activator of peroxymonosulfate for the degradation of antibiotics norfloxacin, Sep. Purif. Technol. 212 (2019) 536–544.
[37] B. Wang, Y.N. Li, L. Wang, Metal-free activation of persulfates by corn stalk biochar for the degradation of antibiotic norfloxacin: activation factors and degradation mechanism, Chemosphere 237 (2019), 124454.
[38] B.M. Liu, W.B. Song, H.X. Wu, Z.Y. Liu, Y. Teng, Y.J. Sun, Y.H. Xu, H.L. Zheng, Degradation of norfloxacin with peroxymonosulfate activated by nanoconfinement Co_3O_4@CNT nanocomposite, Chem. Eng. J. 398 (2020), 125498.
[39] G.L. Peng, M.H. Zhang, S.B. Deng, D.N. Shan, Q. He, G. Yu, Adsorption and catalytic oxidation of pharmaceuticals by nitrogen-doped reduced graphene oxide/Fe_3O_4 nanocomposite, Chem. Eng. J. 341 (2018) 361–370.
[40] G. Wang, D. Zhao, F. Kou, Q. Ouyang, J. Chen, Z. Fang, Removal of norfloxacin by surface Fenton system ($MnFe_2O_4$/H_2O_2): kinetics, mechanism and degradation pathway, Chem. Eng. J. 351 (2018) 747–755.
[41] Z.Y. Chu, T.H. Chen, H.B. Liu, D. Chen, X.H. Zou, H.L. Wang, F.W. Sun, P.X. Zhai, M. Xia, M. Liu, Degradation of norfloxacin by calcite activating peroxymonosulfate: performance and mechanism, Chemosphere 282 (2021), 131091.
[42] G.V. Buxton, C.L. Greenstock, W.P. Helman, A.B. Ross, Critical-review of rate constants for reactions of hydrated electrons, hydrogen-atoms and hydroxyl radicals ($^{\bullet}OH/^{\bullet}O^-$) in aqueous- solution, J. Phys. Chem. Ref. Data 17 (1988) 513–886.
[43] P.S. Rao, E. Hayon, Redox potentials of free radicals. IV. Superoxide and hydroperoxy radicals $^{\bullet}O_2^-$ and $^{\bullet}HO_2$, J. Phys. Chem. 79 (1975) 397–402.
[44] F. Wilkinson, W.P. Helman, A.B. Ross, Rate constants for the decay and reactions of the lowest electronically excited singlet state of molecular oxygen in solution. An expanded and revised compilation, J. Phys. Chem. Ref. Data 24 (1995) 663–1021.
[45] P. Bilski, K. Reszka, M. Bilska, C.F. Chignell, Oxidation of the spin trap 5,5-dimethyl-1-pyrrolineN-oxide by singlet oxygen in aqueous solution, J. Am. Chem. Soc. 118 (1996) 1330–1338.
[46] H. Zhang, J. Joseph, M. Gurney, D. Becker, B. Kalyana, Bicarbonate enhances peroxidase activity of Cu, Zn-superoxide dismutase, J. Biol. Chem. 277 (2002) 1013–1020.
[47] Q.X. Zhang, P. Chen, M.H. Zhuo, F.L. Wang, Y.H. Su, T.S. Chen, K. Yao, Z.W. Cai, W.Y. Lv, G.G. Liu, Degradation of indometacin by simulated sunlight activated CDs-loaded $BiPO_4$ photocatalyst: roles of oxidative species, Appl. Catal. B: Environ. 221 (2018) 129–139.
[48] D.F. Evans, M.W. Upton, Studies on singlet oxygen in aqueous solution. Part 3. The decomposition of peroxy-acids, J. Chem. Soc. Dalton Trans. 6 (1985) 1151–1153.
[49] Y. Zhou, J. Jiang, Y. Gao, S.Y. Pang, Y. Yang, J. Ma, J. Gu, J. Li, Z. Wang, L. H. Wang, L.P. Yuan, Y. Yang, Activation of peroxymonosulfate by phenols: important role of quinone intermediates and involvement of singlet oxygen, Water Res. 125 (2017) 209–218.
[50] C.T. Guan, J. Jiang, C.W. Luo, S.Y. Pang, Y. Yang, Z. Wang, J. Ma, J. Yu, X. Zhao, Oxidation of bromophenols by carbon nanotube activated peroxymonosulfate (PMS) and formation of brominated products: comparison to peroxydisulfate (PDS), Chem. Eng. J. 337 (2018) 1385–8947.
[51] W. Nam, S.J. Back, K.A. Lee, B.T. Ahn, J.G. Muller, C.J. Burrows, J.S. Valentine, Nickel complexes as antioxidants. Inhibition of aldehyde autoxidation by nickel(II) tetraazamacrocycles, Inorg. Chem. 35 (1996) 6632–6633.
[52] W.D. Oh, Z.L. Dong, T.T. Lim, Generation of sulfate radical through heterogeneous catalysis for organic contaminants removal: current development, challenges and prospects, Appl. Catal. B- Environ. 194 (2016) 169–201.
[53] P.J. Duan, Y.F. Qi, S.S. Feng, X.M. Peng, W. Wang, Y. Yue, Y.N. Shang, Y.W. Li, B. Y. Gao, X. Xu, Enhanced degradation of clothianidin in peroxymonosulfate /catalyst system via core-shell FeMn @ N-C and phosphate surrounding, Appl. Catal. B- Environ. 267 (2020), 118717.
[54] A. Jawad, K. Zhan, H.B. Wang, A. Shahzad, Z.H. Zeng, J. Wang, X.Q. Zhou, H. Ullah, Z.L. Chen, Z.Q. Chen, Tuning of persulfate activation from a free radical to a nonradical pathway through the incorporation of non-redox magnesium oxide, Environ. Sci. Technol. 54 (2020) 2476–2488.
[55] J.B. Dan, Q.F. Wang, K. Mu, P.H. Rao, L. Dong, X. Zhang, Z.D. He, N.Y. Gao, J. C. Wang, Degradation of sulfachloropyridazine by UV-C/persulfate: kinetics, key factors, degradation pathway, Environ. Sci. -Water Res. 6 (2020) 2510–2520.
[56] M. Golshan, B. Kakavandi, M. Ahmadi, M. Azizi, Photocatalytic activation of peroxymonosulfate by TiO_2 anchored on cupper ferrite (TiO_2@$CuFe_2O_4$) into 2,4-D degradation: process feasibility, mechanism and pathway, J. Hazard. Mater. 359 (2018) 325–337.
[57] R.X. Yuan, S.N. Ramjaun, Z.H. Wang, J.S. Liu, Effects of chloride ion on degradation of Acid Orange 7 by sulfate radical-based advanced oxidation process: implications for formation of chlorinated aromatic compounds, J. Hazard. Mater. 196 (2011) 173–179.

[58] G.P. Anipsitakis, T.P. Tufano, D.D. Dionysiou, Chemical and microbial decontamination of pool water using activated potassium peroxymonosulfate, Water Res. 42 (2008) 2899–2910.
[59] L.J. Peng, X.G. Duan, Y.N. Shang, B.Y. Gao, X. Xu, Engineered carbon supported single iron atom sites and iron clusters from Fe-rich Enteromorpha for Fenton-like reactions via nonradical pathways, Appl. Catal. B-Environ. 287 (2021), 119963.
[60] L. Yang, C.S. Chen, Y.J. Tu, Y.H. Huang, H. Zhang, Heterogeneous degradation of organic pollutants by persulfate activated by CuO-Fe_3O_4: mechanism, stability, and effects of pH and bicarbonate ions, Environ. Sci. Technol. 49 (2015) 6838–6845.
[61] L. Cheng, M.Y. Wei, L.H. Huang, F. Pan, D.S. Xia, X.X. Li, A.H. Xu, Efficient H_2O_2 oxidation of organic dyes catalyzed by simple copper(II) ions in bicarbonate aqueous solution, Ind. Eng. Chem. Res. 53 (2014) 3478–3485.
[62] J.B. Peng, H.H. Shi, J.H. Li, L.H. Wang, Z.Y. Wang, S.X. Gao, Bicarbonate enhanced removal of triclosan by copper(II) catalyzed Fenton-like reaction in aqueous solution, Chem. Eng. J. 306 (2016) 484–491.
[63] Z.H. Meng, S.H. Wu, S.W. Sun, Z. Xu, X.C. Zhang, X.M. Wang, Y. Liu, H.T. Ren, S. Y. Jia, H. Bai, X. Han, Formation and oxidation reactivity of $MnO_2^+(HCO_3^-)_n$ in the $Mn^{II}(HCO_3^-)$-H_2O_2 system, Inorg. Chem. 59 (2020) 3171–3180.
[64] L. Pi, N. Yang, W. Han, W. Xiao, D.H. Wang, Y. Xiong, M. Zhou, H.B. Hou, X. H. Mao, Heterogeneous activation of peroxymonocarbonate by Co-Mn oxides for the efficient degradation of chlorophenols in the presence of a naturally occurring level of bicarbonate, Chem. Eng. J. 334 (2018) 1297–1308.
[65] G.X. Huang, C.Y. Wang, C.W. Yang, P.C. Guo, H.Q. Yu, Degradation of bisphenol A by peroxymonosulfate catalytically activated with $Mn_{1.8}Fe_{1.2}O_4$ nanospheres: synergism between Mn and Fe, Environ. Sci. Technol. 51 (2017) 12611–12618.
[66] N. Stern, J. Mejia, S. He, Y. Yang, M. Ginder-Vogel, E.E. Roden, Dual role of humic substances as electron donor and shuttle for dissimilatory iron reduction, Environ. Sci. Technol. 52 (2018) 5691–5699.
[67] C. Sun, T. Chen, Q.X. Huang, M.X. Zhan, X.D. Li, J.H. Yan, Activation of persulfate by CO_2-activated biochar for improved phenolic pollutant degradation: performance and mechanism, Chem. Eng. J. 380 (2020), 122519.